CHAPTER 3
NUMERICAL SIMULATION AND PROOF-OF-CONCEPT EXPERIMENT

The work discussed in the chapters subsequent to this will rely heavily on numerical simulations. In this chapter we describe an experiment to ensure that our simulation closely represents real structures which it is designed to simulate. Towards the end of this chapter, we will also understand the need for adaptive modal filters.

3.1 Verification of Digital Filter Model and Gain Matrix Formula

3.1.1 Verification of Digital Filter Model

To verify the method we use to represent the structure with digital filters, we shall present a numerical example. As an example, we simulate a beam with boundary conditions as described in Fig. 2.1, which are a pin at $x = 0$ and a pin and a torsion spring at $x = L$. The properties of the rectangular beam are given in Table 3.1.

Table 3.1 Physical properties of beam

Property	Value	Unit	Property	Value	Unit
Length (L)	0.4382	m	Density (ρ)	2700	kg/m^3
Width (b)	0.0381	m	Young's modulus (E)	$68(10)^9$	Pa
Thickness	3.175	mm	Poisson's ratio	0.3	

With the above physical properties, the parameter $\frac{1}{L^2}\sqrt{\frac{EI}{\rho_L}} = 23.9596$ s^{-1}. The eigenvalues can be computed by solving Eq. (2.2). For several nondimensional torsion spring constant T^* (defined in Eq. (2.1)), these eigenvalues are as shown in Table 3.2. The $T^* = 0$ case is the case of simply supported beam without a torsion spring and is included in the table for comparison.

Table 3.2 Eigenvalues of beam

T^*	0	0.032	0.1	0.32	1	3.2	10	32
λ_1	3.1416	3.1466	3.1572	3.1888	3.2733	3.4461	3.6646	3.8193
λ_2	6.2832	6.2857	6.2911	6.3076	6.3560	6.4769	6.6874	6.8915
λ_3	9.4248	9.4265	9.4301	9.4412	9.4749	9.5657	9.7516	9.9748
λ_4	12.566	12.567	12.570	12.578	12.604	12.676	12.839	13.067
λ_5	15.708	15.709	15.711	15.717	15.738	15.798	15.942	16.167
λ_6	18.849	18.850	18.852	18.857	18.875	18.926	19.054	19.217
λ_7	21.991	21.991	21.993	21.998	22.013	22.057	22.173	22.383
λ_8	25.132	25.133	25.134	25.139	25.152	25.191	25.296	25.498
λ_9	28.274	28.274	28.276	28.279	28.291	28.327	28.422	28.616
λ_{10}	31.415	31.416	31.417	31.420	31.431	31.463	31.551	31.737

The natural frequencies can be computed by Eq. (2.3). For several nondimensional torsion spring constant T^*, the natural frequencies of the beam are as shown in Table 3.3.

Table 3.3 Natural frequencies of beam (Hz)

T^*	0	0.032	0.1	0.32	1	3.2	10	32
f_1	37.6	37.8	38.0	38.8	40.9	45.3	51.2	55.6
f_2	150.5	150.7	150.9	151.7	154.1	160.0	170.5	181.1
f_3	338.7	338.8	339.1	339.9	342.3	348.9	362.6	379.4
f_4	602.2	602.3	602.6	603.4	605.8	612.8	628.6	651.1
f_5	940.9	941.0	941.3	942.1	944.6	951.8	969.2	996.7
f_6	1354.9	1355.0	1355.3	1356.1	1358.6	1366.0	1384.5	1408.1
f_7	1844.1	1844.3	1844.5	1845.3	1847.9	1855.4	1874.8	1910.6
f_8	2408.7	2408.8	2409.1	2409.9	2412.4	2420.0	2440.1	2479.3
f_9	3048.5	3048.6	3048.9	3049.7	3052.2	3059.9	3080.6	3122.7
f_{10}	3763.6	3763.7	3764.0	3764.8	3767.3	3775.0	3796.2	3840.9

For the numerical example, we choose $T^* = 1$ as the torsion spring stiffness. The mode shapes of the beam as computed by Eq. (2.4) are shown in Fig. 3.1.

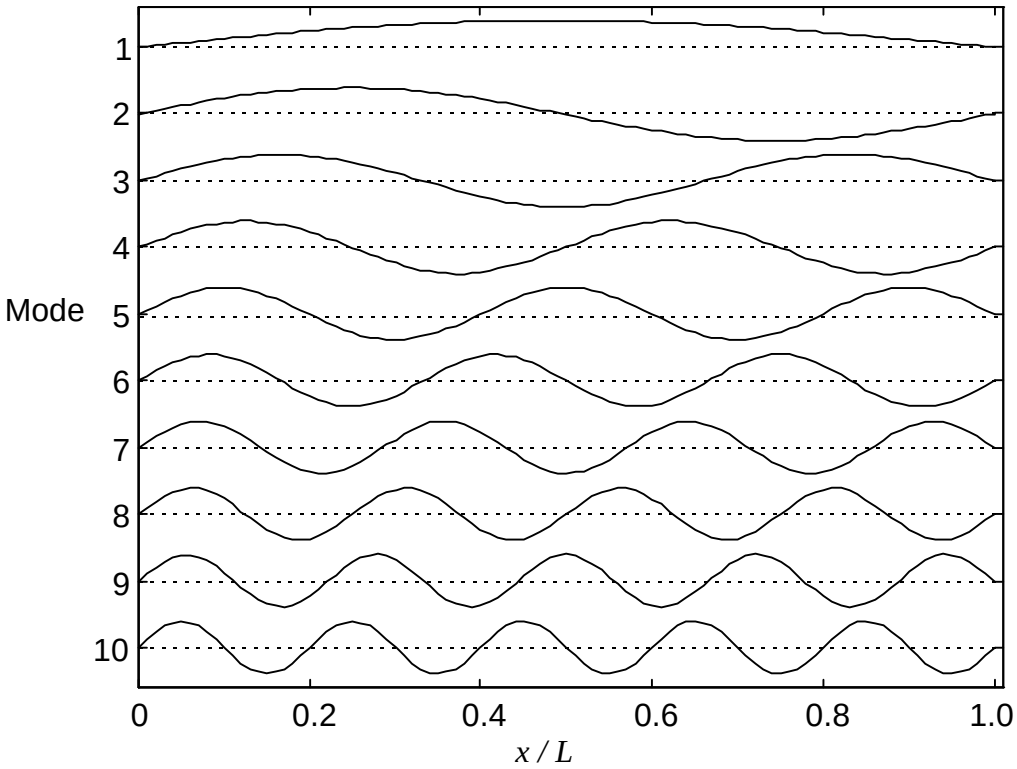

Figure 3.1 Flexural mode shapes of beam.

The beam is excited with a point force at position x_f = 0.1304 times the length of the beam. A typical loss factor value for a metal beam in bending is about 0.001 (Lazan, 1968). However, the beam that we will use in an experiment described later in this dissertation is covered on one side with a thin polymer double-sided adhesive tape and with segments of polyvinylidene fluoride (PVDF) film. An experiment described later in a subsection 3.2.3 was used to estimate the damping ratio of the beam with this covering. The damping ratios for all modes was found to be around ζ_m = 0.01. With the above properties, we can compute the driving-point mobility of the beam using Eq. (2.7) and Eq. (2.8). We limit our calculation to include only the first 10 modes of the beam.

To simulate the beam, we can design a digital filter that consists of a bank of IIR filters with coefficients computed by Eqs. (2.17) through (2.19). We chose a sampling rate 4 times the tenth natural frequency f_{10}. As shown in the z-plane in Fig. 3.2.a, the filter poles are barely inside the unit circle because the damping ratios are quite low. Figure 3.2.b shows the filter denominator coefficients are very close to the unstable region above the $a_2 = 1$ line.

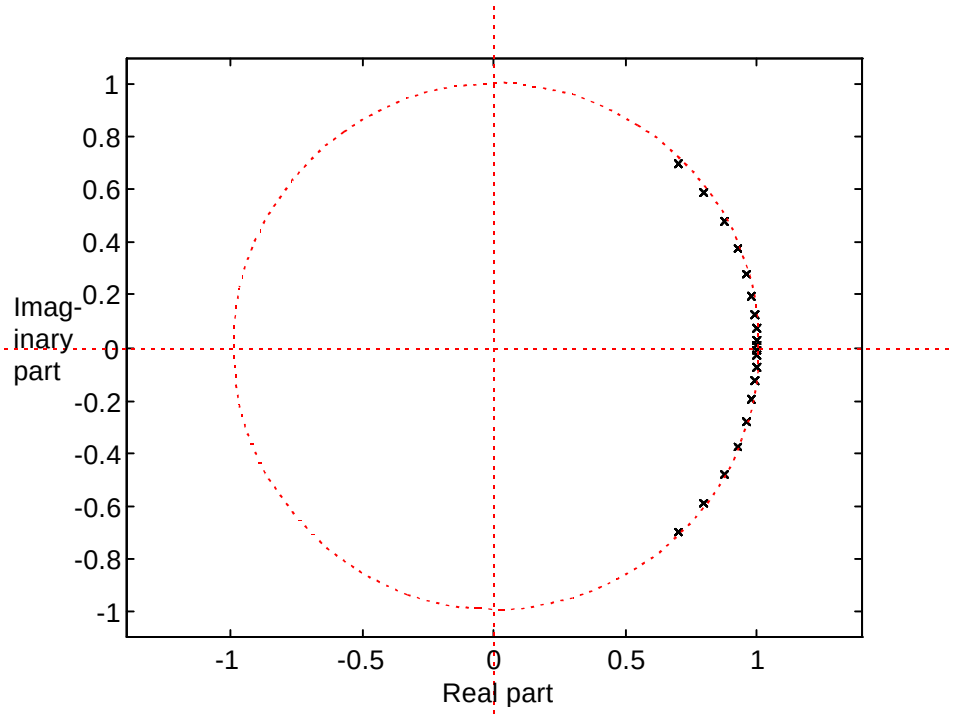

a)

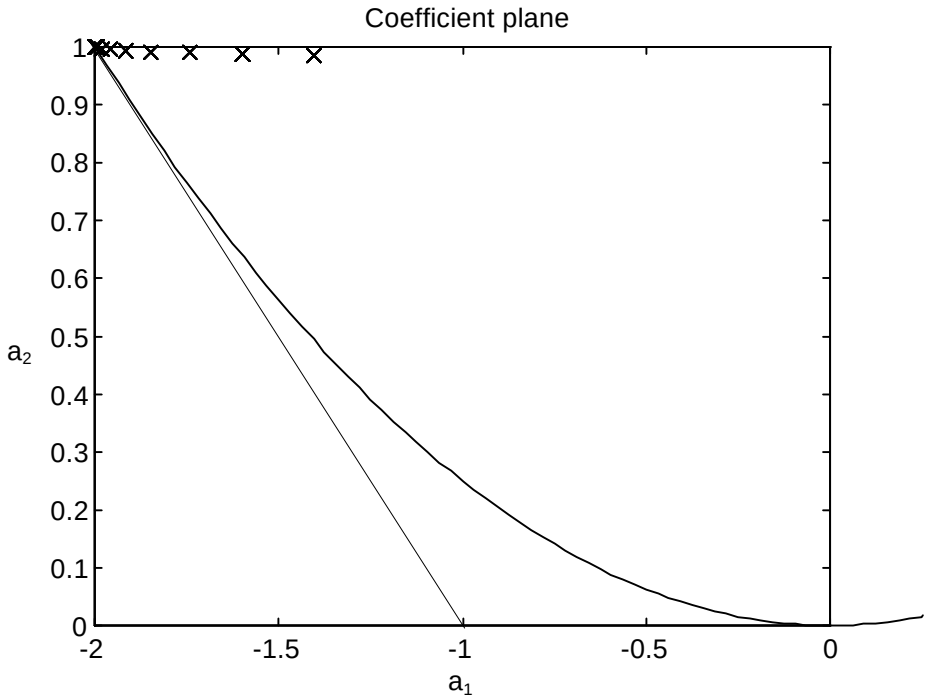

b)

Figure 3.2 a)*Z*-plane poles b)Denominator coefficients of the IIR-filter-equivalent of the beam.

To verify that the parallel bank of digital filters, indeed, simulates the driving-point mobility of the beam, we compare the continuous-time driving-point mobility of the beam with the FRF of the IIR filter. The driving point mobility of the structure is computed by substituting $s = j\omega$ into Eq. (2.14) and the Laplace transform of Eq. (2.7). The FRF of the filter can be computed by substituting $z = \exp(j\omega T)$ into Eq. (2.23). The comparison between the beam's driving-point mobility and the IIR filter's FRF is shown in Fig. 3.3. The magnitudes of the two FRF's agree very well. However, the digital filter loses about 60^o of phase at the high end of the frequency range. Such a phase lag might be of some importance in a feedback control system design. A higher sampling rate would bring the phase back up.

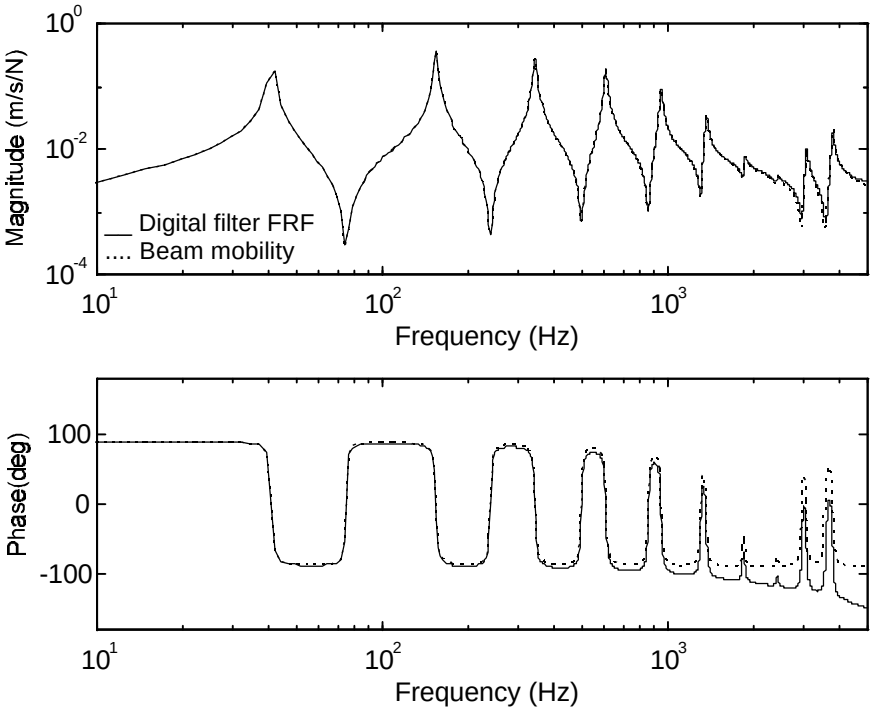

Figure 3.3 Comparison between beam's driving-point mobility and digital filter's FRF.

Further verification of the digital filter characteristics can be done by comparing the impulse response of the filter to the impulse response of the beam. Other excitation than an impulse force could be used as well. We choose the impulse force because it is mathematically the simplest excitation in the integration of the modal equation of motion.

The modal response of the beam to a unit impulse force $\delta(t)$ can be obtained as follows. Integrating the modal equation of motion between $t = 0$ and $t = \varepsilon$, and taking the limit as $\varepsilon \to 0$, we obtain

$$\dot{\eta}_m(0^+) = \phi_m(x_f) \tag{3.1}$$

The magnitude of the initial modal coordinate happens to be the same as the mass-normalized mode shape value at the excitation point. (However, it can be shown that the unit is not $kg^{-1/2}$ but $kg^{1/2}\ ms^{-1}$, due to the integral of $\delta(t)$ over time. The corrected unit is consistent with the modal equation of motion.) Using the above initial modal coordinate as an initial condition and

$$\eta_m(0) = 0 \tag{3.2}$$

as another initial condition, we can show that the modal coordinate as a response to the impulse force is

$$\dot{\eta}_m(t) = \phi_m(x_f)\exp(-\zeta_m\omega_m t)\left\{\omega_{dm}\cos(\omega_{dm}t) - \zeta_m\frac{\omega_m}{\omega_{dm}}\sin(\omega_{dm}t)\right\} \tag{3.3}$$

where

$$\omega_{dm} = \omega_m\sqrt{1-\zeta_m^2} \tag{3.4}$$

is the damped natural frequency of mode-*m*.

The impulse response of each IIR filter can be evaluated in the discrete-time domain using Eq. (2.20). The unit impulse is approximated with an input of 1/(sampling period) at $k = 0$ and zero inputs thereafter. We can compare the responses of the digital filters with the modal responses of the beam. The comparison is shown in Fig. 3.4. The agreement between the digital filter outputs and ideal modal coordinates is very good. This agreement confirms that the parallel bank of second-order IIR filters in Fig. 2.3, indeed, represents the dynamics of the beam with specified modal properties.

3.1.2 Verification of Gain Matrix Formula

From the above comparison in frequency domain and in time domain, we have established confidence in simulating the beam with a parallel bank of second-order digital filters. Since we can simulate the responses of the beam, we can also simulate the outputs of the piezoelectric segments on the beam. Now we can design a modal sensor for the beam by computing a gain weight matrix **W** that will transform the outputs of the piezoelectric segments into modal coordinates. We will take into account the first ten modes of the structure, use ten segments, and obtain a sensor that outputs the first ten modal coordinates of the structure. Equation (2.37) gives the segment output matrix $\mathbf{C}_S$. The m^{th} column of this matrix represents the contribution of the m^{th} mode to the outputs of the sensor segments. These columns are shown graphically as strips in Fig. 3.5. We can see that low-numbered modes contribute less to the outputs of the segments than high-numbered

modes. This difference is understandable since the output of a segment is related to the deflection slope rather than the deflection itself. Higher modes generally give more slopes than lower modes.

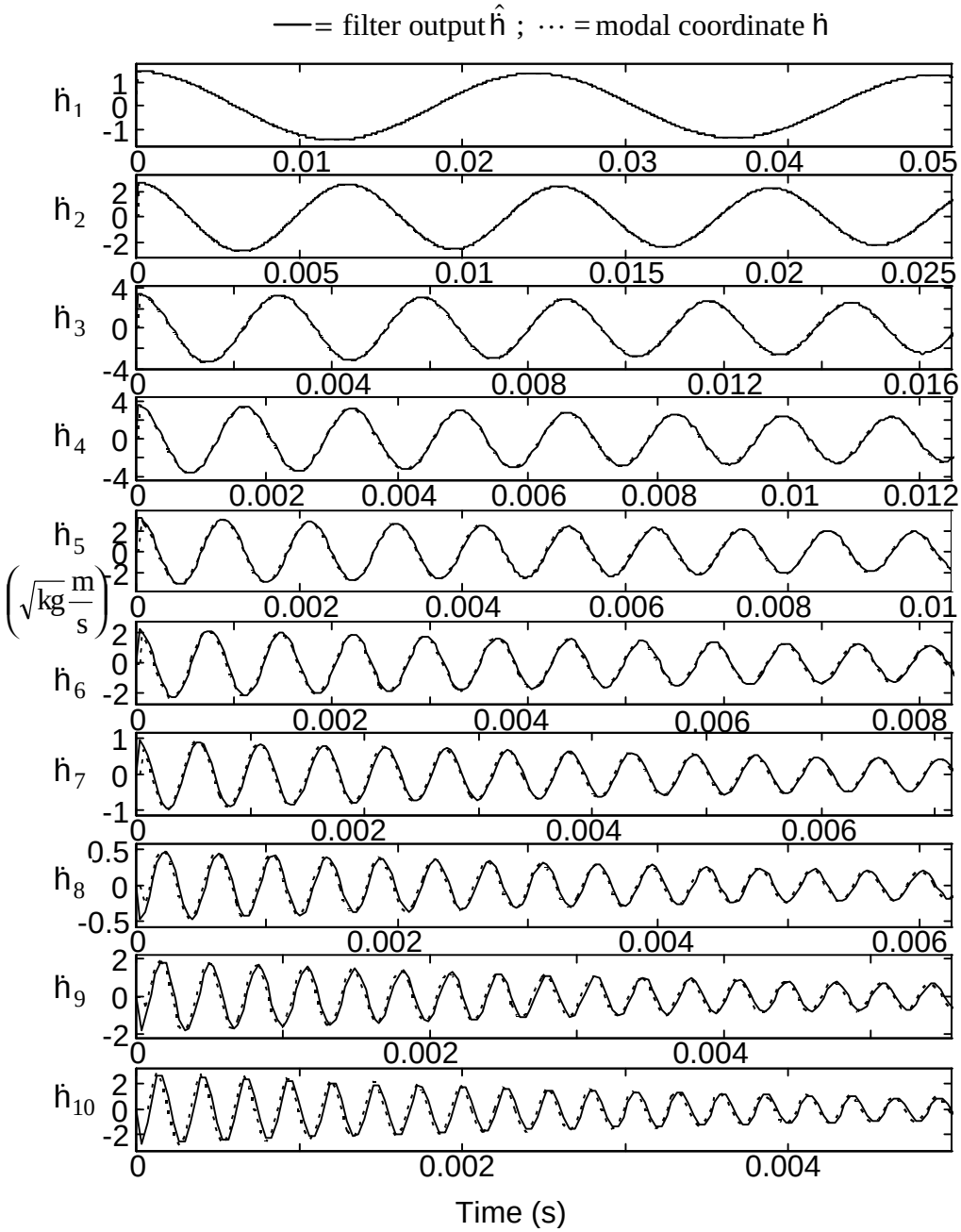

Figure 3.4 Time-domain comparison between second-order digital filters and ideal modal coordinates: impulse response.

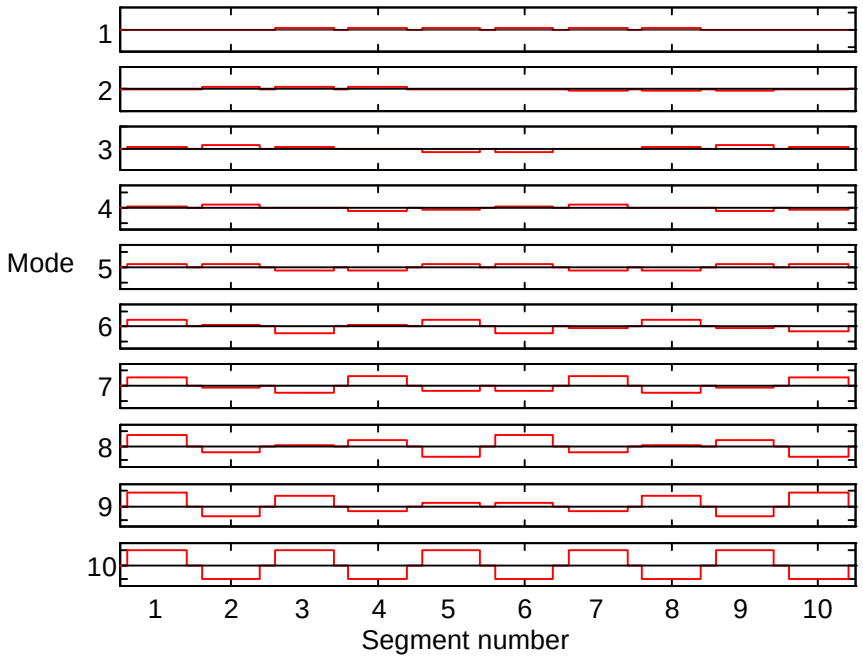

Figure 3.5 Contribution of each mode to segment outputs.

Finally, we compute the sensor gain matrix **W** according to Eq. (2.40). This gain matrix is shown in Table 3.4. Each row of this matrix contains the gains for each mode, and is shown as a strip in Fig. 3.6. If we multiply the outputs of the segments by this gain matrix according to Eq. (2.39), the product will approximate the modal coordinates of the beam.

The mode-1 sensor has big gains compared to other modal sensor. These gains are large mainly because the contribution of mode 1 to the outputs of the segments is small, as shown in Fig. 3.5.

Table 3.4 Gain matrix for modal sensor.

2.008	5.8254	9.0594	11.389	12.589	12.547	11.278	8.922	5.7183	1.9872
0.929	2.4178	2.9356	2.2640	0.6490	-1.293	-2.818	-3.339	-2.655	-1.014
0.6441	1.4021	1.0110	-0.191	-1.192	-1.146	-0.080	1.1269	1.4764	0.6726
0.4748	0.7601	-0.024	-0.798	-0.495	0.4539	0.7222	-0.072	-0.831	-0.502
0.3845	0.3860	-0.375	-0.364	0.4041	0.3962	-0.365	-0.345	0.4222	0.4007
0.3178	0.1166	-0.399	0.1167	0.3053	-0.335	-0.130	0.3757	-0.150	-0.334
0.2743	-0.046	-0.211	0.3094	-0.134	-0.126	0.3132	-0.207	-0.028	0.2860
0.2388	-0.150	-0.002	0.1417	-0.244	0.2326	-0.159	-0.007	0.1341	-0.251
0.2129	-0.190	0.1552	-0.095	0.0397	0.0383	-0.089	0.1596	-0.183	0.2244
0.0948	-0.096	0.0939	-0.097	0.0932	-0.098	0.0925	-0.100	0.0923	-0.101

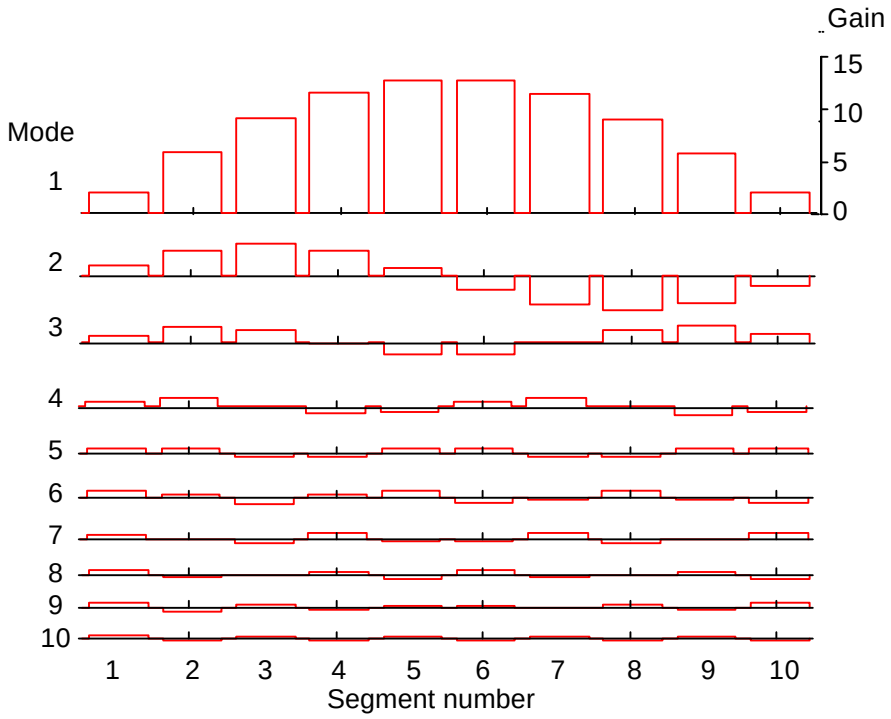

Figure 3.6 Gain matrix for modal sensors.

To verify that the gain matrix **W** really produces modal coordinates when multiplied by the segment outputs, we shall do the following test.

1. Apply an impulse force to the beam with zero initial conditions.
2. Compute the ideal modal response for each mode by solving the modal equation of motion (Eq. (2.8)) in time domain.
3. Compute the (time-domain) velocity response along the beam.
4. Compute the segment outputs using Eq. (2.36).
5. Multiply the segment outputs by the gain matrix to obtain the modal sensor output.
6. Compare the results of step 5 with the result of step 2.

Steps 1 and 2 were done earlier with Eq. (3.3) (see Fig. 3.4). The outputs of the segments (step 4) can be computed using Eq. (2.35) through (2.37). The sensor gain matrix is obtained using Eq. (2.40). In this step we use 10 modes to obtain the gain matrix for 10 segments. The impulse responses of the modal filter $\dot{\hat{\eta}}$ is compared with the ideal modal coordinates $\dot{\eta}$ in Fig. 3.7.

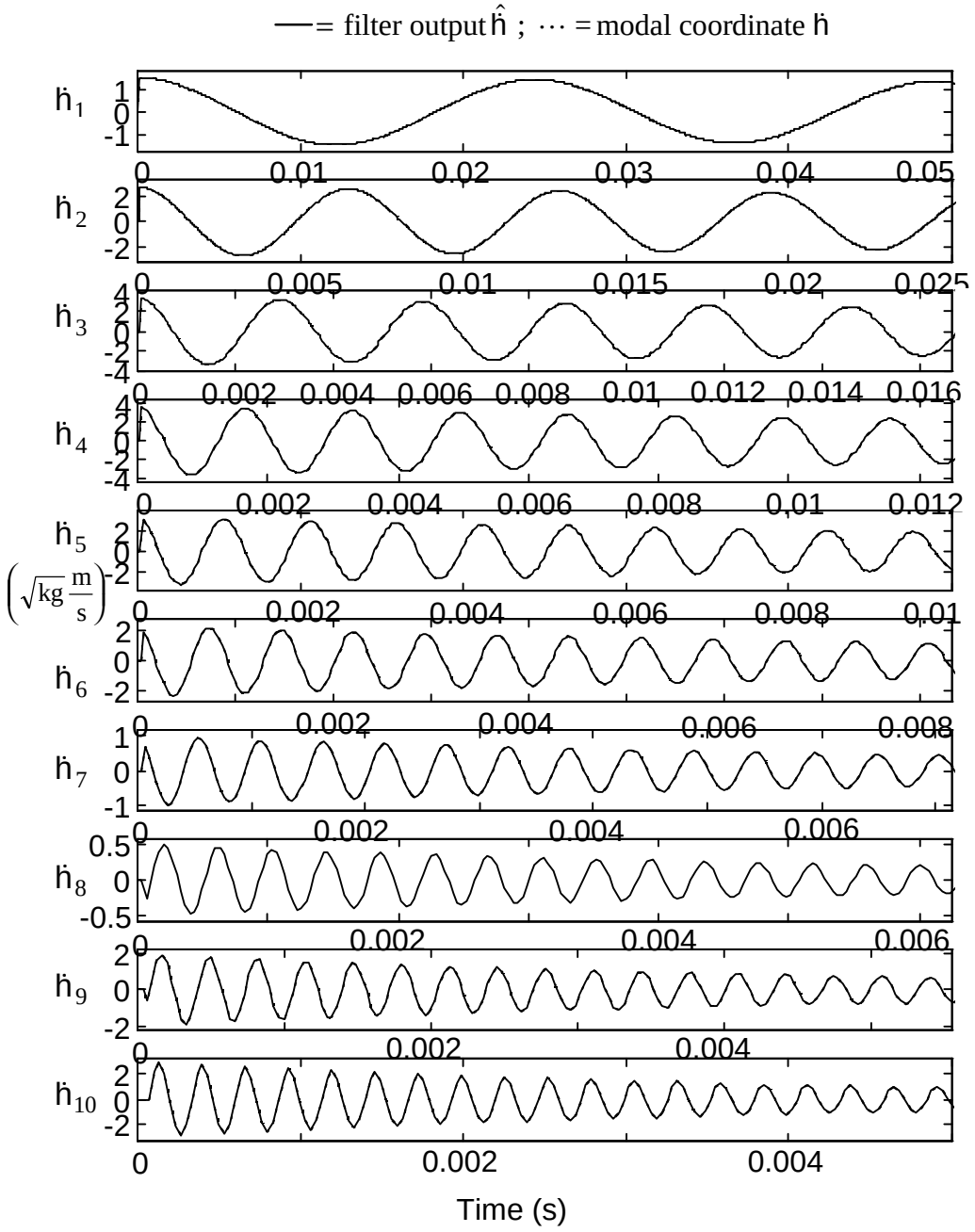

Figure 3.7 Modal sensor outputs compared to ideal modal coordinates: impulse responses.

3.1.3 Modal Truncation and Spatial Aliasing

As mentioned in subsection 2.3.3, the gain matrix calculation in Eq. 2.40 is approximate in nature. Ideal modal coordinates can only be sensed with an infinite number of segments (i.e., Lee's modal sensor as in Fig. 1.5, with perfect geometry for the mode shapes). Using a finite number of segments means using a finite number of modes in Eq. (2.37) and (2.40). This modal truncation results in non-ideal modal coordinates. To investigate the effect of modal truncation, this time we include the first 12 modes of the beam in the response calculation. The natural frequencies of these modes are f_{11} = 4558 Hz and f_{12} = 5423 Hz. The modal damping ratios are assumed to be 0.01. We use the gain matrix in table 3.4 to obtain the outputs of the modal sensors (step 5). This gain matrix was calculated using only 10 modes. The outputs of the modal sensors are shown in Fig. 3.8. These outputs are generally in excellent agreement with the ideal modal coordinates, except for modes 8 and 9, which are not shown in Fig. 3.8.

The outputs of mode-8 and mode-9 sensors are shown Fig. 3.9. These outputs do not agree with the ideal modal coordinates. The disagreement is shown further in the frequency domain in Fig. 3.10.

Figure 3.9 shows that modes 8 and 9 sensors are very sensitive to modes 11 and 12. It can be shown that if mode 13 were included in the beam response, this mode will be sensed by mode 7 sensor. This is a clear indication of spatial aliasing. This problem could be solved in spatial domain by altering the shapes of the segments, or in frequency domain by using analog low-pass filters. The frequency domain solution simply means filtering out the signal contribution from modes with higher indices than the modes used in the gain matrix calculation. Spatial aliasing problem needs special treatment outside the scope of this dissertation. For now, we just conclude that we should low-pass filter the sensor output before the samplers, or that we should use band-limited excitation forces so that aliasing is not a problem.

The above numerical simulation shows that the linear combiner is very effective in separating the response of the beam into its modal coordinates. Experiments are required at this point of the research work to verify the concept and numerical simulation. After experimental verification, we shall be ready to develop an algorithm that would adjust the gain matrix automatically so that we would not need to know the modal properties of the structure to create the modal sensor. Development of this algorithm will be the main thrust of this dissertation.

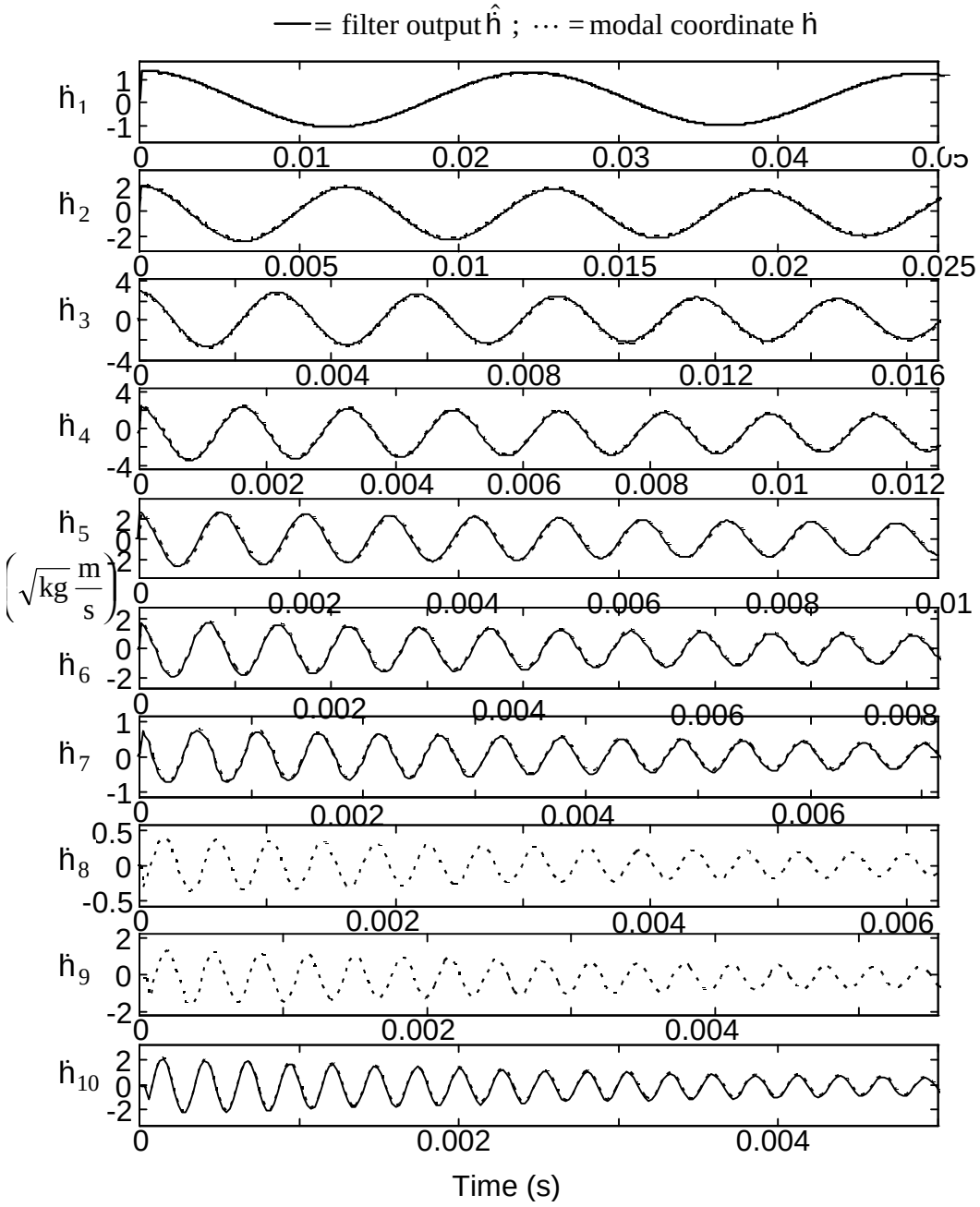

Figure 3.8 Responses of a 10-mode filter to a 12-mode impulse excitation.

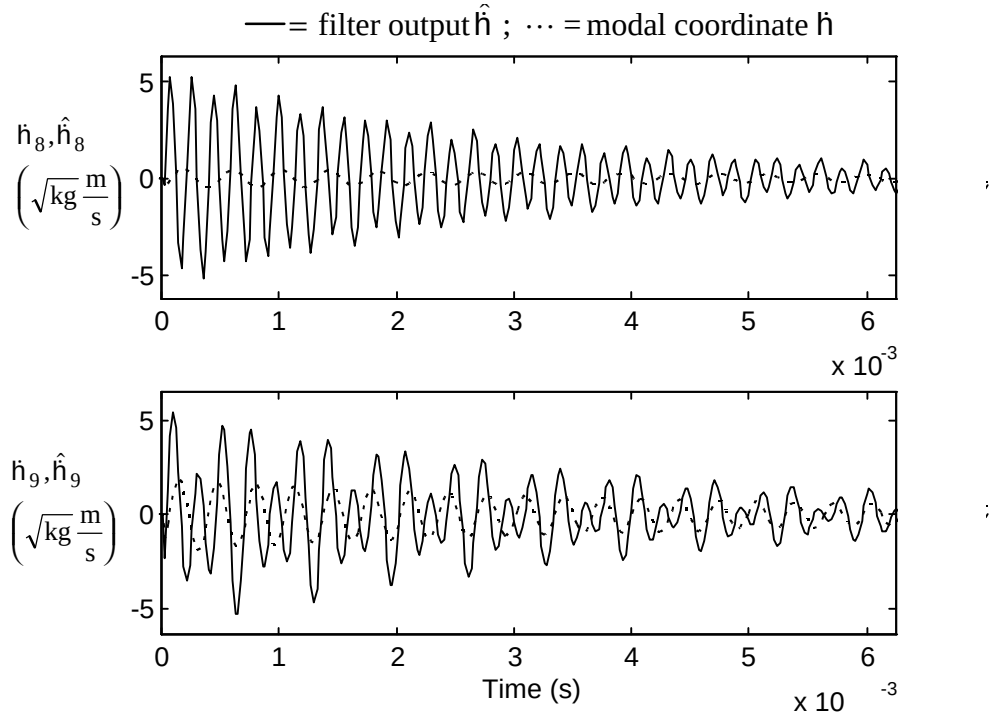

Figure 3.9 Modal sensor output compared to ideal modal coordinates: impulse responses of modes 8 and 9

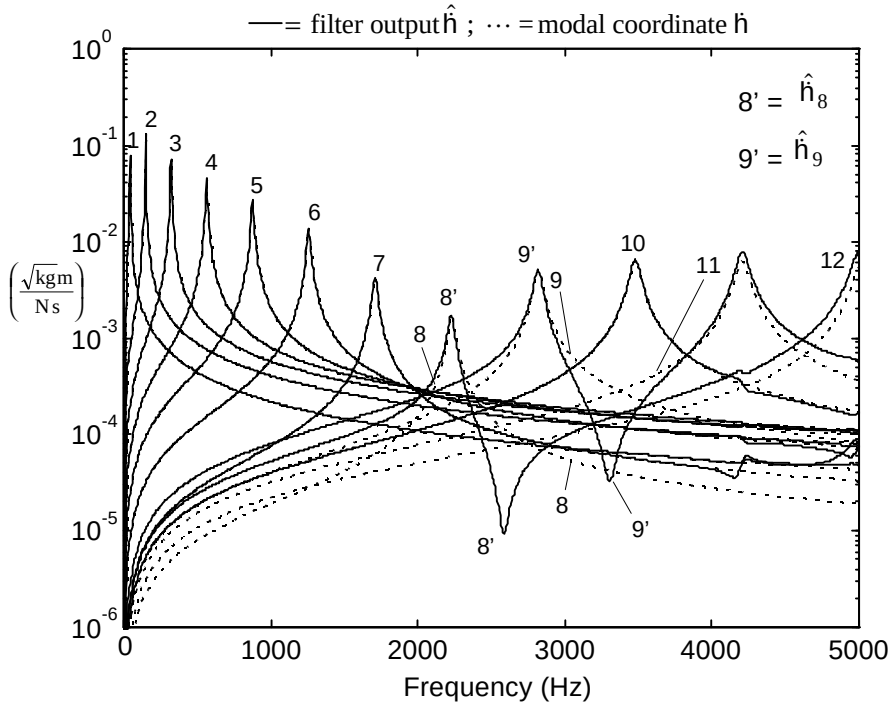

Figure 3.10 Modal sensor output compared to ideal modal coordinates: FRF's from force to sensor outputs and to modal coordinates.

3.2 Proof-of-Concept Experiment

In the above section we verified the method we use to represent the structure with digital filters. We also and also demonstrated numerically that the gain matrix calculated by Eq. (2.40), indeed, transforms the segment outputs into modal coordinates. In this section, we will further verify the simulation technique and the gain matrix calculation method by performing an experiment with a simply supported beam equipped with piezoelectric film segments.

3.2.1 Properties of Experimental Structure

For the experiment, we use a beam with approximated pin supports at $x = 0$ and at $x = L$. The properties of the beam are as tabulated in Table 3.5.

Table 3.5 Physical properties of beam

Property	Value	Unit	Property	Value	Unit
Length (L)	0.4500	m	Density (ρ)	2700	kg/m^3
Width (b)	0.0381	m	Young's modulus	68(10)^9	Pa
Thickness	3.175	mm	Poisson's ratio	0.3	

The shaker point of action is at $x_f = 0.1742$ m.

This structure can be considered a special form of the structure in Fig. 2.1 with $T^* = 0$. For this case, the modal properties of the structure can be found in many texts such as Blevins (1984). The natural frequencies of the beam are

$$\omega_m = \frac{1}{L^2}\sqrt{\frac{EI}{\rho_L}}\,\lambda_m^2 \tag{3.5}$$

where ρ_L is the mass per unit length of the beam. The m^{th} eigenvalue is

$$\lambda_m = m\pi . \tag{3.6}$$

With the above physical properties, the parameter $\frac{1}{L^2}\sqrt{\frac{EI}{\rho_L}} = 21.0455$ s^{-1}, and the beam's analytical natural frequencies are as shown in Table 3.6.

Table 3.6 Analytical natural frequencies of beam (Hz)

f_1	f_2	f_3	f_4	f_5	f_6	f_7	f_8	f_9	f_{10}	f_{11}	f_{12}
37.6	150.5	338.7	602.2	940.9	1355	1844	2409	3049	3764	4554	5420

The mass-normalized mode shapes of the beam are

$$f_m(x) = \sqrt{\frac{2}{r_L L}} \sin\left(\frac{m\pi x}{L}\right). \tag{3.7}$$

The m^{th} modal coordinate $\eta_m(t)$ is the solution to the equation of motion, which is

$$\ddot{\eta}_m(t) + 2\zeta_m \omega_m \dot{\eta}(t) + \omega_m^2 \eta(t) = f_m(x_f) f(t) \tag{2.8}$$

where ω_m^2 is the eigenvalue, ζ_m denotes the modal damping, $f_m(x_f)$ is the value of the mass-normalized mode shape at the forcing point position. The summation limit M in Eq. (2.7) is set to 12.

The ideal responses from force to the sensor outputs are computed as follows. To simulate the modal coordinates in frequency domain, we use MATLAB's *bode* command with a state space representation of the structure. The state space model is given in Eqs. (2.9) through (2.13).

To compute the FRF's from force to segment output voltages, we use Eq. (2.36). Then we compute the gain matrix **W** using Eq. (2.40). Finally, we compute the FRF from force to sensor output using Eq. (2.39). Obviously, these ideal sensor outputs are identical to the modal coordinates. In the next sections, we will compare the experiment results with these ideal sensor outputs.

3.2.2 Experimental Setup

Figure 3.11 shows the setup for the experiment, where we can see the beam covered with PVDF segments attached to the steel frame. In the background we can see the shaker and the signal conditioning circuit.

Figure 3.12 explains the setup in detail. Thin metal "shim" is used to connect each end of the aluminum beam to the frame. This shim gives almost no resistance to bending, but is very stiff in the beam's transverse direction. Therefore, the shim approximates a simple boundary condition. The shaker excites the beam at position $x = x_f$. A force transducer is placed between the shaker's stinger and the beam.

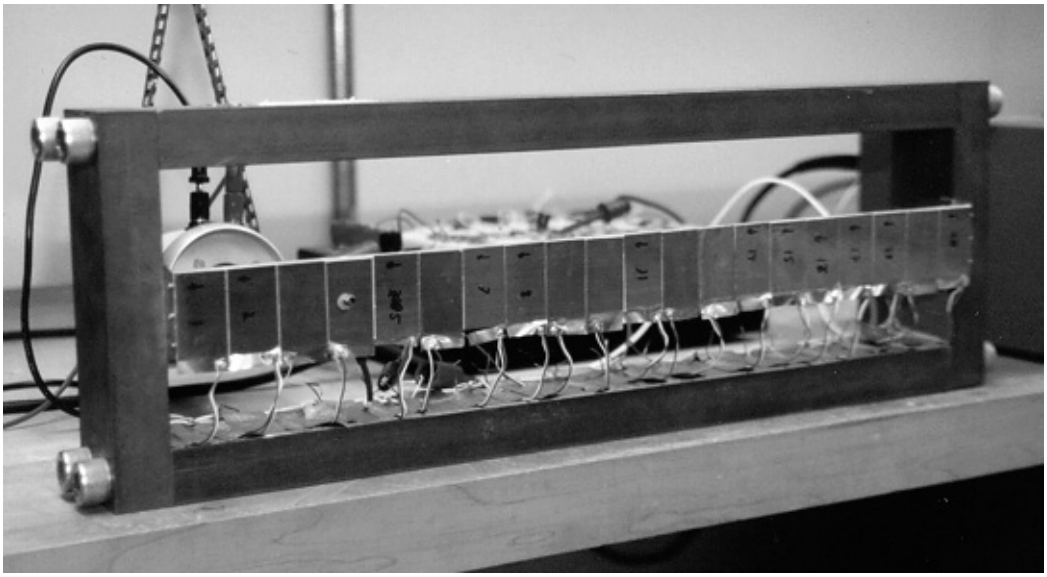

Figure 3.11 Experimental setup.

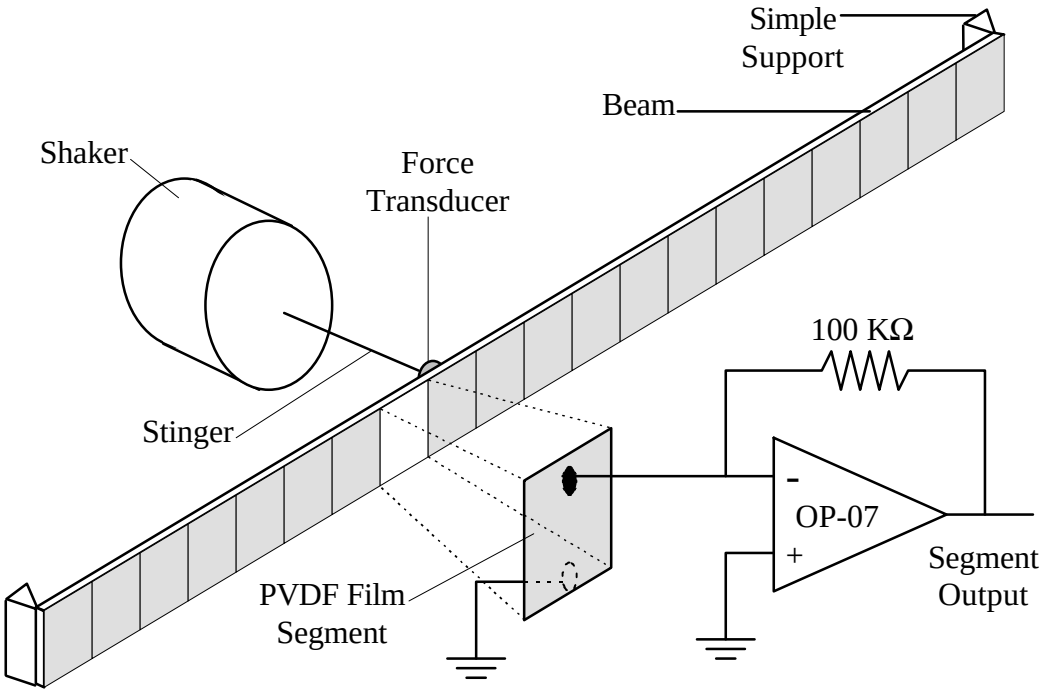

Figure 3.12 Schematic picture of experiment setup.

The beam is covered with N = 20 segments of piezoelectric polyvinylidene fluoride (PVDF) film. Each piezoelectric film segment is connected to a current amplifying circuit shown in the figure. This circuit is designed so that the output signal is proportional to the strain rate of the segment (Lee, 1991). The input impedance of this circuit is theoretically zero. Current flows freely from and to the PVDF film segment. The operational amplifier (Op Amp) used is type OP-07. The 100 kΩ feedback resistor multiplies the current to produce the output voltage. A Tektronix 2630 Fourier Analyzer receives the force transducer signal and the segment outputs. A frequency range of 0-3 kHz is chosen. Above this range, the experiment rig did not give very clean resonance peaks in the FRF's.

The experiment in the 2-3kHz range was done with swept-sine excitation for two reasons: 1) to ensure clean FRF's and 2) to prevent aliasing. The spatial resolution of the segmented sensor is finite, which means that higher mode vibrations can be sensed falsely as lower mode vibrations. Of course, limiting the excitation frequency below the upper limit of the calculation frequency range still excites the modes above the frequency range. However, it is expected that the modal residues of the higher modes excited this way will be lower than the modal residues of the modes within the frequency range. From Table 3.6, we see that eight modes can be studied in this range.

3.2.3 Experiment Results

The magnitudes of the FRF's from force to the outputs of the segments are shown in Fig. 3.13.

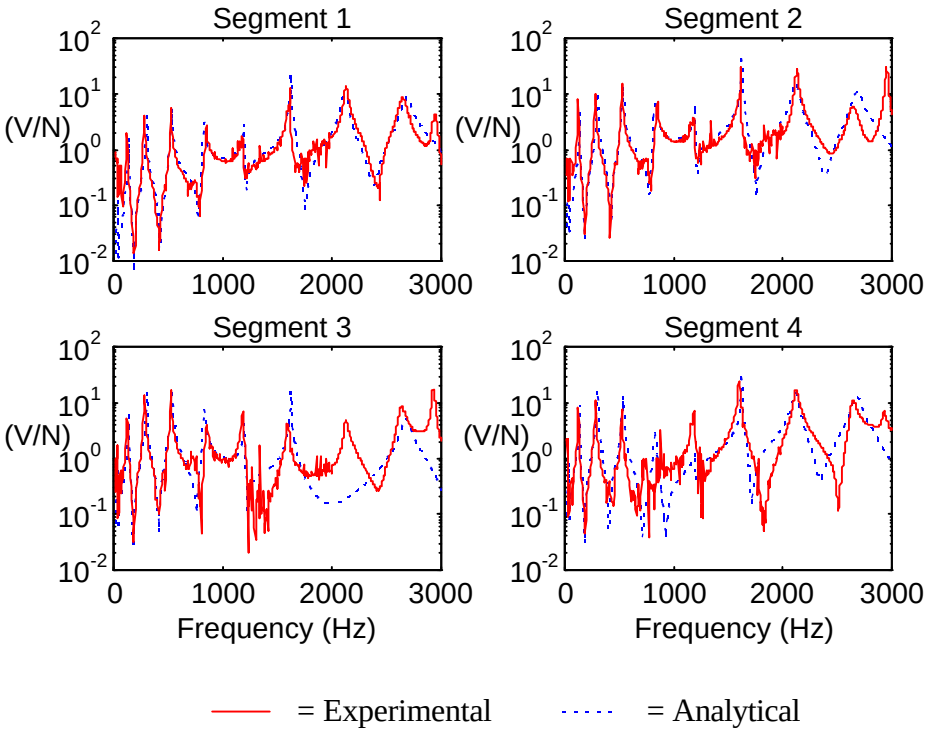

Figure 3.13 Magnitude responses from force to segment outputs

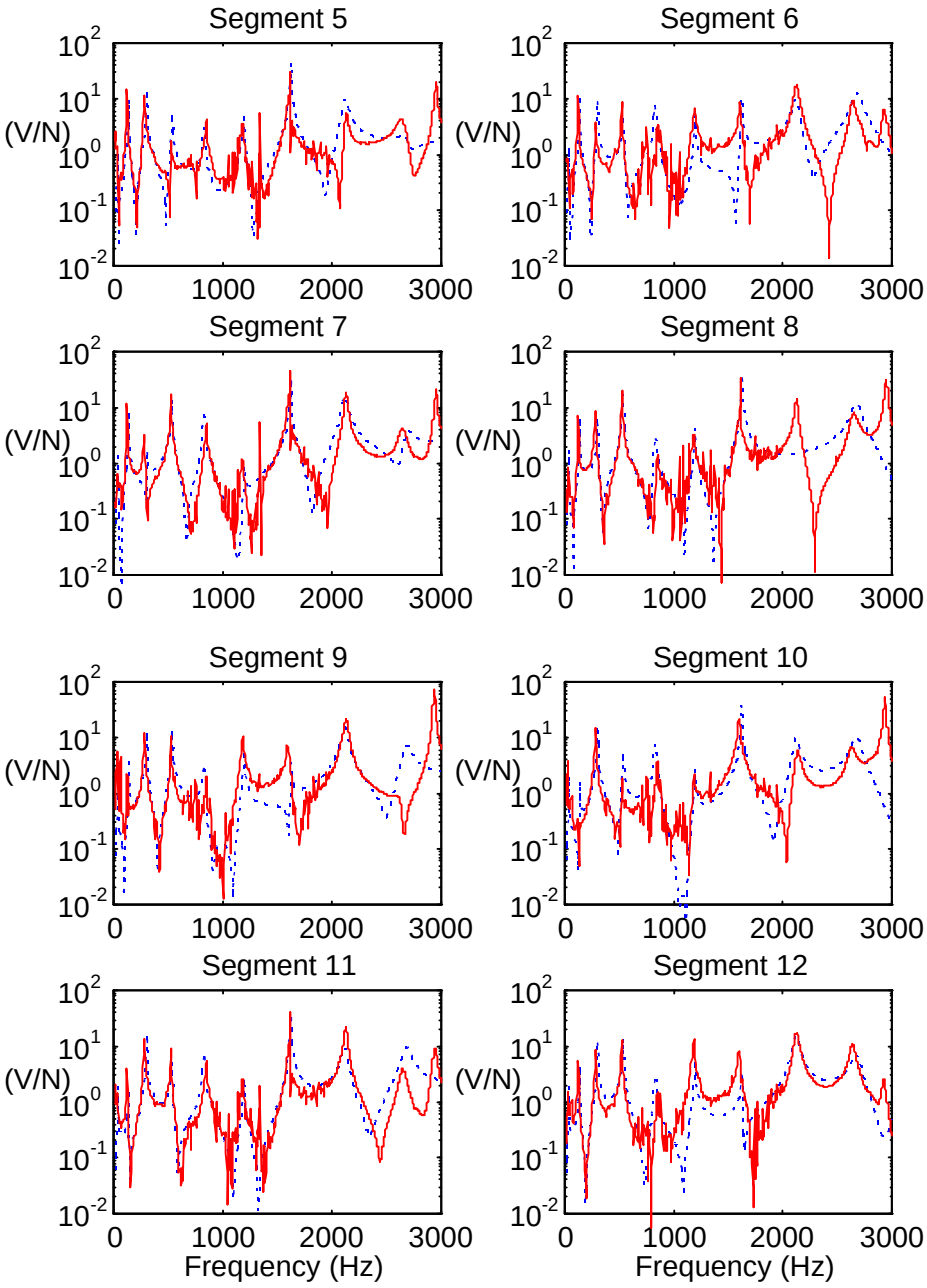

Figure 3.13 Magnitude responses from force to segment outputs

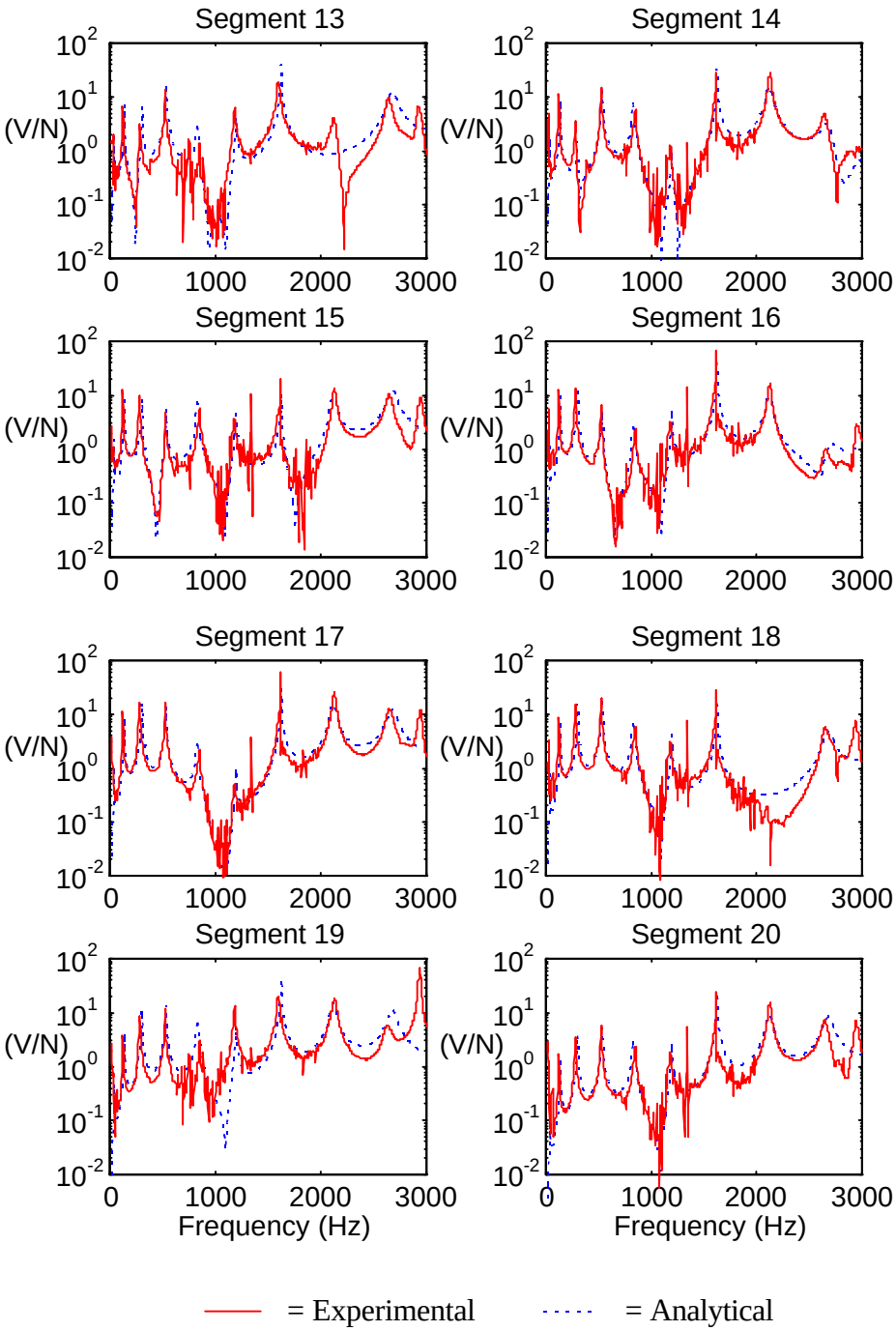

Figure 3.13 Magnitude responses from force to segment outputs

As we can see in Fig. 3.13, the experimentally obtained outputs of the individual segments are very close to the predicted outputs. The modal damping ratios in the theoretical calculation (0.01 for all modes) were actually obtained by trial and error so that the anti-resonances of the FRF's predicted by theoretical calculation agreed with those obtained by this experiment.

The discrepancies between the experiment results and the analytical prediction in the 2k-3kHz range is caused partly by the difference in the actual beam natural frequencies from the predicted natural frequencies. The prediction gave lower frequencies than the experimental beam. The thin metal shims at the ends of the beam may have added rotational stiffness to the boundary condition, violating the zero-moment assumption. The ninth resonance, which was captured by the experiment, was not even predicted to be in the frequency range. Spatial aliasing, i.e., contribution from higher modes which are not accounted for by the theoretical prediction, may have caused the extra resonance peak in segment 13.

A small area around the shaker point of action caused a near field that was not predicted by the theory. This local effect added to the deviation of the segment FRF's from the ideal FRF's. The force transducer was attached to the beam by bolting to a whole through the beam. The force transducer and its attachment loaded the beam and added local stiffness, thereby altering the mode shapes. The mode shapes with small wavelength were affected most. This was likely to be why the experiment FRF's differ from the theoretical FRF's in the frequency range above 2 kHz.

Despite the discrepancies, each experimentally-obtained FRF from force to segment output generally agrees well with the predicted FRF. The next step is to calculate the sensor gain matrix **W** by Eq. (2.40). Because we use 20 segments, we use $M = 20$ in Eqs. (2.37) and (2.40) so that we obtain a 20-by-20 gain matrix. However, we only managed to capture the first eight resonances in the experiment. The higher mode resonances did not show a good 180^o phase rolloff. For this reason we only include the lowest eight modes in further calculation. In other words, we only use the first eight rows of the gain matrix **W** and convert the outputs from 20 segments into eight modal coordinates. The first eight rows of **W** are shown graphically in Fig. 3.14.

3.2.4 Discussion on Experiment Results

The sensor outputs are calculated from the segment outputs using Eq. (2.32). The magnitudes of the FRF's from force to sensor outputs are shown in Fig. 3.15.

Figure 3.15 shows that the sensor outputs resulting from transforming the segment outputs with the theoretically calculated gain matrix **W** exhibit some modal filtering effects, especially for mode 4 and mode 8. The highest response peaks always occur at the resonance frequency corresponding to the intended modes. The responses tend to be lower at frequencies away from the intended resonance frequencies. However, for each mode there are several resonance peaks at natural frequencies of other modes than the intended one.

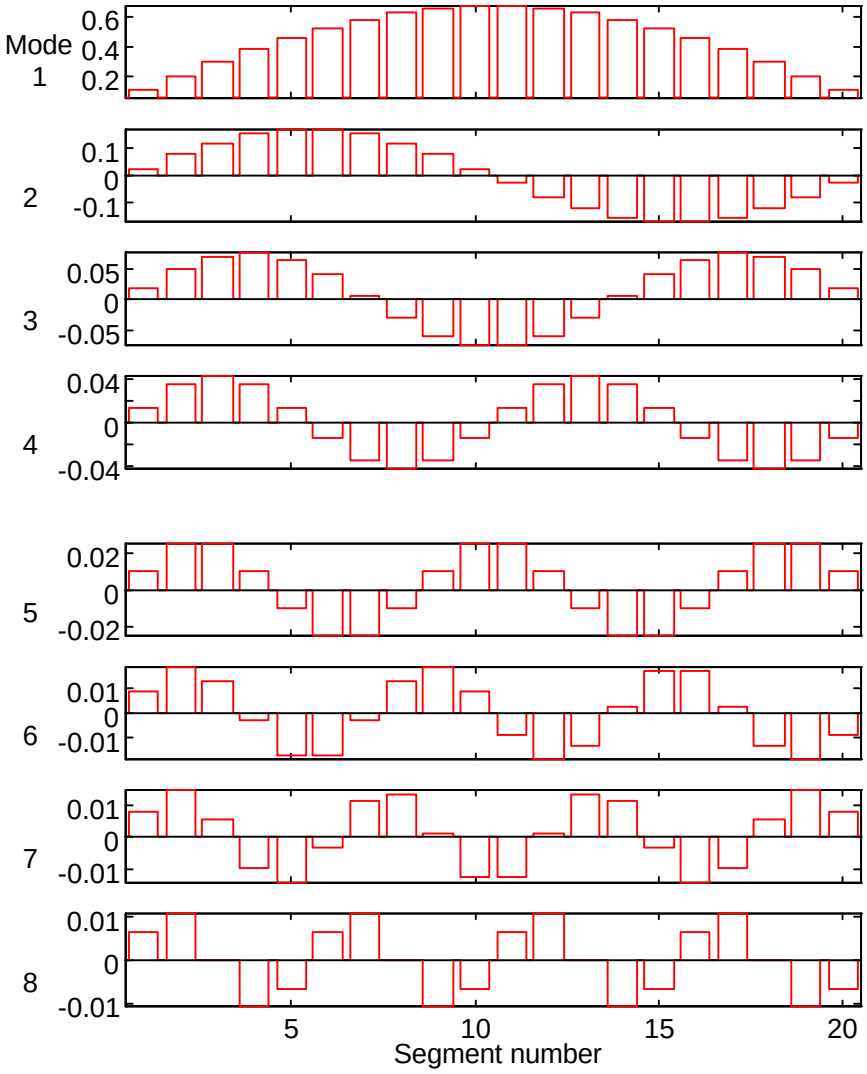

Figure 3.14 Sensor gain matrix **W** for transforming 20 segment outputs into 8 modal coordinates.

An unconventional method to show modal filtering effect, used in what is likely to be the most famous treatise of modal filtering theory is to plot the sensor responses in linear scale (Lee, 1987). Replotting Fig. 3.15 with this method visually accents the modal filtering effects. In Fig. 3.16, it appears more clearly that the sensor outputs do tend to emulate modal coordinates. For most of the modes, the outputs of the linear combiners are close to the desired single-mode outputs. Most of the mode sensors show responses in some agreement with the predicted responses. They are very sensitive to the mode that they are designed to sense.

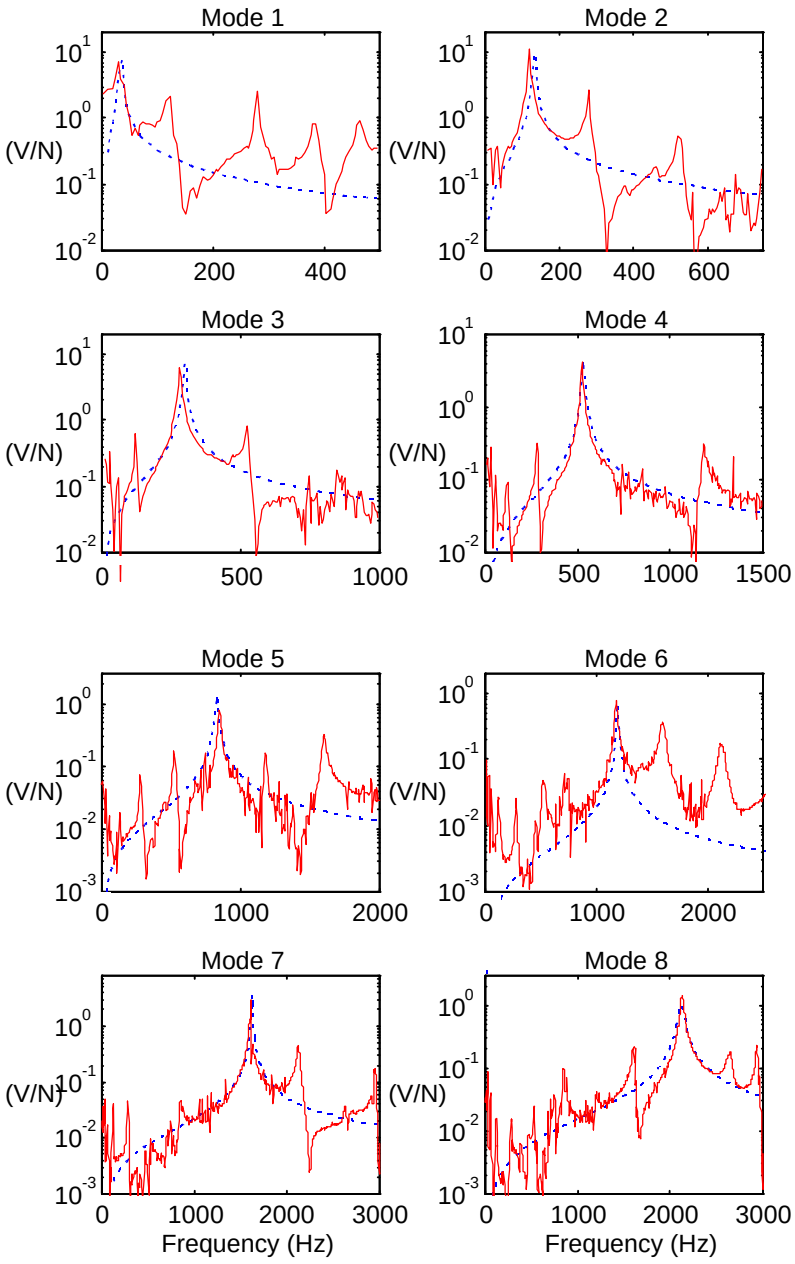

Figure 3.15 Magnitude responses from force to sensor outputs.

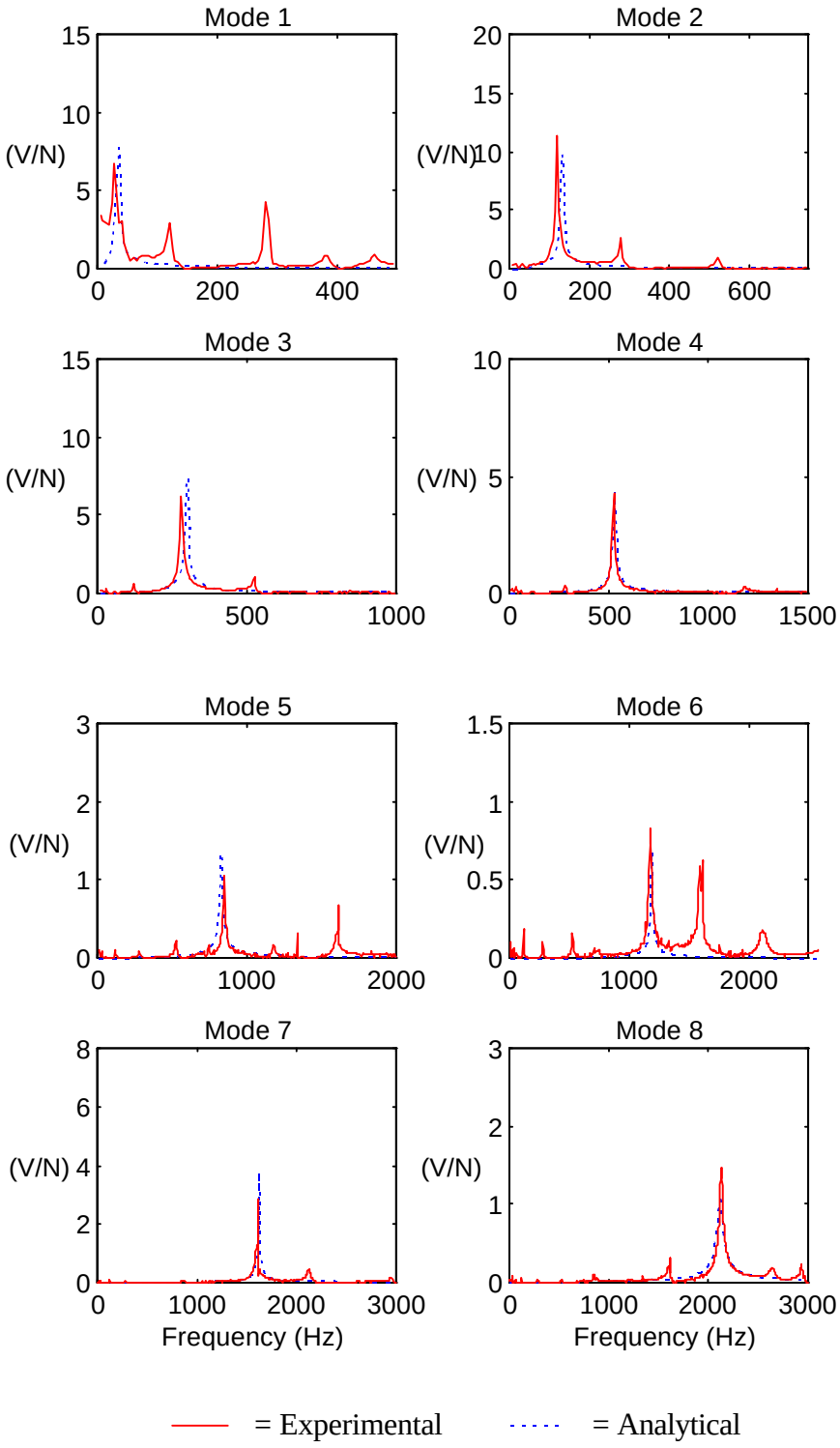

Figure 3.16 Magnitude responses from force to sensor outputs: linear scale.

Figure 3.17 End connection to approximate simple support.

The modal filters are also sensitive to other modes than the intended ones. The worst case is the mode-1 sensor, which seems to fail to filter out other modes than mode-1. This imperfect modal filtering effect can be attributed to the following inaccuracies:

The segments were cut and attached by hand. They did not have perfect geometry and were not attached in the perfect positions. Lee (1990) showed that even microscopic imperfection in a shaped film sensor resulted in rather significant imperfection in modal filtering effects.

The boundary conditions of the beam were not ideal simple supports. The beam was attached to a frame with thin sheet metal pieces attached to ends of the beam with small screws. This connection, shown in Fig. 3.17, does not give zero resistance to bending. The mode shapes of the beam were not exactly as predicted by the theory.

The point force causes evanescent (near-field) modes around the point of force application. These modes were never accounted for in the theory, but may actually contribute more than negligibly to the vibration of the beam. Additionally, the force transducer was attached to the beam by drilling a hole through the beam and bolting the force transducer to the hole. This attachment creates

extra stiffness around the hole and some mass loading on the beam. The actual modes of the experimental beam are different from the theoretically predicted modes.

Many other factors may have contributed to the imperfect modal filtering effects. However, in general we can conclude that the theory of modal filtering with segments of piezoelectric film has been somewhat supported by the simple experiment. We can also conclude that any imperfection in the knowledge of the actual mode shapes and in the construction of the sensor may result in severe ‘leaking’ of the modal filters.

A method to improve this modal filtering technique in is to incorporate adaptive digital signal processing algorithm to adjust the segment weights automatically based on the sensed imperfections in the modal filtering effects. This method of improvement is the main thrust of the remainder of this dissertation.

3.3 Chapter Summary

This chapter established confidence in the models and simulation procedures developed in chapter 2. Numerical and experimental verification of the models and procedures showed the following:

1. Simulations both in time and frequency domains showed that the parallel second-order digital filter model agrees with the dynamic model of the structure.

2. Frequency-domain responses obtained by the experiment have verified:1) The digital filter model of the beam. 2)The model for the responses of all sensor segments.

3. Transformation of experimental segment outputs by theoretical gain matrix showed that the ideal gain matrix transforms the segment outputs into modal coordinates, albeit imperfectly. Unintended modes are not completely filtered out by the modal filters.

4. Spatial aliasing is a problem that must be avoided in using the segmented sensor.